*Clays and Clay Minerals*, Vol. 61, No. 3, 258–276, 2013.

# THE RATE AND MECHANISM OF DEEP-SEA GLAUCONITE FORMATION AT THE IVORY COAST–GHANA MARGINAL RIDGE

ANDRE BALDERMANN[1,2], LAURENCE N. WARR[2], GEORG H. GRATHOFF[2], AND MARTIN DIETZEL[1]

[1] Institute of Applied Geosciences, Graz University of Technology, 8010 Graz, Austria
[2] Department of Geography and Geology, Greifswald University, 17493 Greifswald, Germany

**Abstract**—The environmental conditions and reaction paths of shallow-water glauconitization (<500 m water depth, ~15ºC) close to the sediment–seawater interface are generally considered to be well understood. In contrast, the key factors controlling deep-sea glauconite formation are still poorly constrained. In the present study, green grains formed in the recent deep-sea environment of the ODP Site 959, Ivory Coast–Ghana Marginal Ridge, (~2100 m water depth, 3–6ºC) were investigated by X-ray diffraction and electron microscopic methods in order to determine the rate and mechanism of glauconitization.

Green clay authigenesis at Hole 959C occurred mainly in the tests of calcareous foraminifera which provided post-depositional conditions ideal for glauconitization. Within this organic-rich micro-environment, Fe-smectite developed <10 ky after deposition of the sediments by precipitation from precursor gels containing Fe, Mg, Al, and silica. This gel formation was supported by microbial activity and cation supply from the interstitial solution by diffusion. At a later stage of early marine diagenesis (900 ky), the Fe-smectites reacted to form mixed-layer glauconite-smectite. Further down (~2500 ky), almost pure glauconite with no compositional gaps between the Fe-smectite and glauconite end members formed. This burial-related Fe-smectite-to-glauconite reaction indicates that the glauconitization process was controlled mainly by the chemistry of the interstitial solutions. The composition of the interstitial solution depends heavily on micro-environmental changes related to early diagenetic oxidation of biodegradable (marine) organic matter, microbial sulfate reduction, silicate mineral alteration, carbonate dissolution, and Fe redox reactions. The availability of Fe is suggested as the probable limiting factor for glauconitization, explaining the various states of green-grain maturity within the samples, and this cation may be the most important rate-determining element.

The rate of glauconite formation at ODP Site 959 is given by $\%Gl_{Sed} = 22.6 \cdot \log(age_{Sed}) + 1.6$ ($R^2 = 0.97$) where $\%Gl_{Sed}$ is the state of glauconitization in the sediment and $age_{Sed}$ is the sediment age (in ky). This glauconitization rate depends mainly on continuous cation supply (in particular Fe) and is about five times less than that in shallow-shelf regions, suggesting significantly slower reaction at the lower temperature of deep-sea environments.

**Key Words**—Deep-sea Sediment, Fe-smectite, Glauconite, Interstitial Solution, Micro-environment, Mixed-layer Clay Minerals, ODP Site 959.

## INTRODUCTION

The formation of glauconite, a dioctahedral, green, Fe-rich 2:1 illite mineral and mixed-layer glauconite-smectite (Gl-S) generally takes place in low-latitude, shallow-marine shelf regions at Eh ~0 mV, seawater pH (8.2), and low sedimentation rates (*e.g.* Odin and Fullagar, 1988). The presence of organic-rich, semi-confined micro-environments such as in foraminifera tests and in fecal pellets is considered to be a key factor for glauconitization, providing suitable post-depositional conditions (*e.g.* Odin and Matter, 1981; Baldermann *et al.*, 2012). In this respect, the occurrence of shallow-water glauconites formed in <500 m water depth, at temperatures below 15ºC (Odin and Fullagar, 1988), and close to the sediment–seawater interface (Wiewióra *et al.*, 2001) represents the typical environment of glauconite formation.

In contrast, exotic occurrences of green-clay authigenesis and glauconite formation have been described in some low-temperature (<6ºC), deep-sea (>1000 m water depth) settings (*e.g.* Buatier *et al.*, 1989; Giresse and Wiewióra, 2001; Gaudin *et al.*, 2005; Cuadros *et al.*, 2011). Such cold environments differ significantly from that of the shallow shelf, with reduced hydrodynamic energy, limited supply and reflux of particular (silicate) mineral phases, low reaction rates, and less microbial activity (*e.g.* Schulz and Zabel, 2006). The effects of these parameters on the glauconitization reaction are still poorly known and only a few constraints are placed on the rates and mechanism of green-clay genesis in such recent deep-sea environments. Gaudin *et al.* (2005) proposed that initially formed Fe-montmorillonite alters rapidly towards the glauconite end member during early marine diagenesis in which the availability of Al and K and the low temperature are the most important rate-controlling factors for glauconitization.

* E-mail address of corresponding author:
baldermann@tugraz.at
DOI: 10.1346/CCMN.2013.0610307

Sediments from the ODP Site 959, Ivory Coast–Ghana Marginal Ridge, provide a condensed and undisturbed sedimentary record without long periods of sediment erosion. Since at least the Miocene, foraminifera and nanofossil oozes have accumulated which are mixed with green grains and minor amounts of detrital silicates (*e.g.* Mascle *et al.*, 1996). Based on petrographic, mineralogical, and geochemical analyses on separated bulk green-grain fractions, Giresse and Wiewióra (2001) and Wiewióra *et al.* (2001) established the authigenic nature of the green clay minerals in these sediments and determined their overall composition to be dioctahedral $Fe^{3+}$-montmorillonite, with minor proportions of interstratified Gl-S (~20% glauconite layers and ~80% Fe-smectite layers) in the more mature, dark green grains. Based on the association of green clay and the occasional periods of sediment erosion, those authors proposed that the authigenic clay formed primarily at the water–sediment interface during phases of intense ion exchange with the seawater. The formation of glauconitic minerals was, therefore, expected to occur immediately after deposition of the sediments and not related to any burial or diagenetic reactions within the sediment pile. The glauconitization mechanism proposed was that of Fe-smectite-to-glauconite alteration *via* the formation of Gl-S.

In the present study, the mineralogical, geochemical, and structural changes that occurred during deep-water glauconitization at the ODP Site 959 were documented in detail and burial-related changes in the development of glauconite are highlighted which have not been described to date in a deep-sea environment. Based on the depth-related changes in the maturity of the green clay minerals and interstitial solution chemistry, the rate and mechanism of glauconite formation are assessed and a reaction model is presented.

## GEOLOGICAL SETTING

The Ivory Coast–Ghana continental margin is located in the eastern equatorial Atlantic Ocean (western Africa) and consists of two major segments. The northern segment is known as the Deep Ivorian Basin (synonymous with the Ivory Basin), an extensional margin that includes the eastern Ivorian continental slope and the southwestern Ghanaian upper slope (Figure 1). The southern segment bounds the Ivory Basin toward the south in a NE–SW direction and is referred to as the Ivory Coast–Ghana Marginal Ridge: a feature 130 km long and 25 km wide (Mascle *et al.*, 1996). Owing to its moderate distance from the surrounding coastlines (~120 km), only a minor proportion of the terrigenous sediment input (suspension load) has reached Site 959C (Giresse and Wiewióra, 2001).

Sediment cores from the Ivory Coast–Ghana Marginal Ridge were recovered during the Ocean Drilling Program (ODP) Leg 159, Site 959, in ~2100 m water depth and at 3–6ºC seawater temperature. The sediments are of particular interest because of their slow (~1–2 cm/ky) and continuous sedimentation rate from at least the Miocene to the Holocene (Wagner, 1998). Due to the elevated position of this site (Latitude: 3º37.669‘N, Longitude: 2º44.116‘W), large hiatuses caused by deep-sea bottom currents or gravity-flow activity are almost absent (Figure 1).

The upper 25 m of ODP Site 959, Hole C, consists of thin dark gray to greenish sedimentary layers of

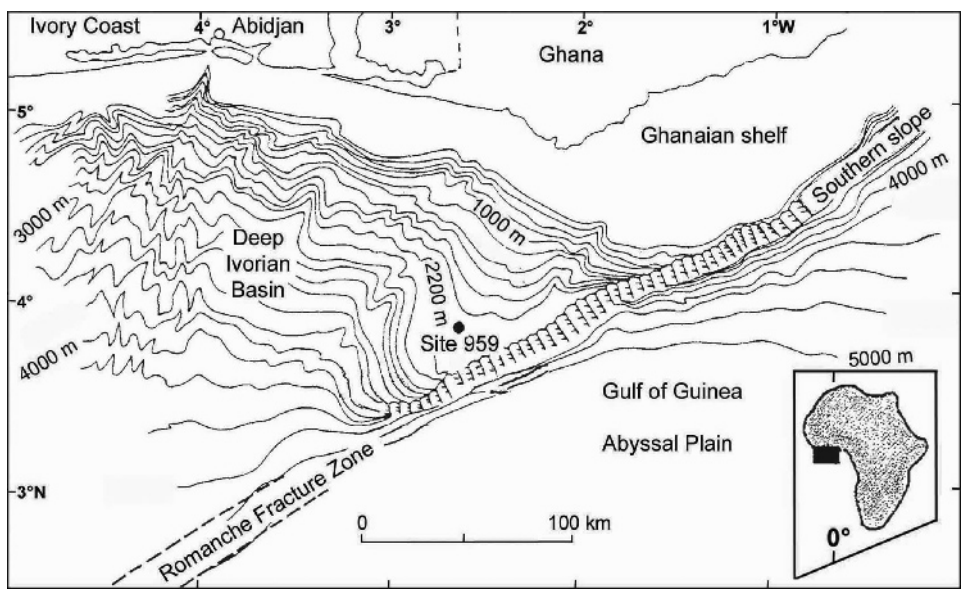


Figure 1. Location map of the ODP Site 959 situated on a small plateau on the Ivory Coast–Ghana Marginal Ridge (western equatorial Africa) (modified after Wiewióra *et al.*, 2001).

https://doi.org/10.1346/CCMN.2013.0610307 Published online by Cambridge University Press

interbedded foraminifera and nanofossil oozes mixed with detrital quartz, feldspar, and clay minerals as well as radiolarians (bio-opal) forming darker horizons (Giresse *et al.*, 1998, Wagner, 1998, Wiewióra *et al.*, 2001). The brighter intervals rich in foraminifera tests frequently contain authigenic green clay and also pyrite infillings. Generally, the beds show a lack of sedimentary structures except for two scour contacts and small bioturbation features.

Stratigraphic classification of Hole 959C was derived from stable oxygen isotope records established on the basis of the epibenthic foraminifer *Cibicides wuellerstorfi* (Wagner, 1998). The $\delta^{18}O$ signal provides a nearly complete record over the last 25 oxygen isotope stages corresponding to the last ~1 My, with one notable stratigraphic gap of ~80 ky near 1.5 meters below the sea floor (mbsf). A longer hiatus of ~530 ky occurs at 11.9 mbsf which is slightly below oxygen isotope stage 25 (Wagner, 1998).

Sediments from the Hole 959C are, thus, suitable for high-resolution study of the recent, green-clay authigenesis and for establishing the roles of deep-water chemistry, provenance, and composition of original sediment, and early marine carbonate diagenesis (*e.g.* Giresse *et al.*, 1998; Norris, 1998; Wagner, 1998).

## MATERIALS AND METHODS

### *Sampling and preparation*

Bulk-sediment samples (21 in total), ~30 $cm^3$ in size, were taken from the upper 25 m of Hole 959C, the core of which is stored at the Bremen Core Repository (MARUM), Germany. This sampled section comprises a sedimentary sequence ranging from Early Holocene (0.16 mbsf, ~0.01 My) to Late Pliocene age (24.91 mbsf, ~2.5 My). Four sub-samples from 1.32, 10.23, 11.49, and 24.91 mbsf were impregnated with epoxy resin to study the microstructure of the green clay infillings in the foraminifera tests by optical microscopy of thin sections. For further mineralogical and chemical analyses of the bulk sediment and green-grain fraction, air-dried sediments were treated with 10% acetic acid for 1 h to dissolve carbonates. The proportion of the green-grain fraction was calculated by weighing the carbonate-free >32 μm size fraction which also contained <5 wt.% quartz, radiolarians, and pyrite. In order to investigate the glauconitization process, ~50 mg of green grains were separated by hand picking under a binocular microscope from the pale to light green, the medium green, and the dark green-grain sub-fractions of samples taken at 0.16, 11.69, and 24.91 mbsf.

### *X-ray diffraction*

X-ray diffraction (XRD) analyses were carried out for mineral identification and quantification using a Bruker D8 Advance instrument (Karlsruhe, Germany) equipped with a Cu-target tube (40 kV, 30 mA), Ni-filter, 0.5º divergence slit, and a scintillation detector. Finely ground bulk samples were prepared (side-loaded) for random powder analyses and run over the range 4–65º2θ using a step size of 0.02º2θ/s with a count time of 1 s/step. Rietveld-based phase quantification was carried out using the PANalytical X'Pert *HighScore Plus* software (developed by PANalytical B.V.). The accuracy of these results was verified by comparison with mass-balance calculations based on X-ray fluorescence (XRF) data of the bulk sediment. Idealized compositions for orthoclase, albite, clinochlore (chlorite), Na-montmorillonite (smectite), and muscovite were assumed for the calculations (Baldermann, 2012). The deviation of the XRD and XRF calculations, expressed as error bars, were <5 wt.% for kaolinite, calcite, and quartz, and <3 wt.% for feldspar, smectite, chlorite, and illite/muscovite. The percentage of glauconite layers (%Gl) in Gl-S was determined on the separated green-grain sub-fractions using oriented preparations. Oriented mounts were made by dispersion of 40 mg of green clay matter in 5 mL of ethanol and ultrasonic treatment for 10 min and then pipetting the clay-in-suspension onto 2 cm × 2 cm glass slides which were subsequently left to air dry overnight. Preparations were run over the range 3–30º2θ using a step size of 0.02º2θ/s and a count time of 0.5 s/step. The %Gl was calculated based on XRD patterns of ethylene glycol (EG)-solvated preparations, according to the equation $\%Gl = 60.8 \cdot d_{EG}002 - 504.5$ which was obtained from *NEWMOD*-calculated %illite in illite-smectite *vs.* $d_{EG}002$ peak position relations reported by Moore and Reynolds (1997). The peak reproducibility of the $d_{EG}002$-reflection was 0.01 Å, equivalent to an analytical precision of ±2%Gl in Gl-S. Results were compared with *Sybilla*© (developed by Chevron-Texaco) calculations to verify the accuracy of the %Gl estimations. For *Sybilla*© modeling, an illite-smectite structure with a large Fe content of 1.2 atoms per formula unit (a.p.f.u.) was assumed, based on $O_{10}(OH)_2$, in the octahedral sites.

### *Scanning and transmission electron microscopy*

In order to study mineral alterations and dissolution features related to early marine diagenesis, ~40 hand-picked, C-coated grains from 0.16 (the least altered state) and 24.91 mbsf (the most altered state) were analyzed by scanning electron microscopy (SEM) using a Jeol JXA-840A. For material disaggregation, the bulk sample was first treated with hydrochloric acid (for 1 h) to remove carbonates.

Transmission electron microscopy (TEM) was undertaken to determine the composition, form, and structure of clay-mineral particles in the separated green-grain sub-fractions from 0.16, 11.69, and 24.91 mbsf using a Jeol JEM 1210 instrument equipped with an Oxford Instruments Pentafel Link-Model 6635 detector. The sample preparation was the same as described by Baldermann *et al.* (2012). Imaging, energy-dispersive

https://doi.org/10.1346/CCMN.2013.0610307 Published online by Cambridge University Press

X-ray spectroscopy (EDX), and selected area electron diffraction (SAED) analyses were performed on single clay-mineral particles using a 200 kV accelerating voltage and 10 s count time to reduce $K^+$ migration. The analytical error of elemental analysis depends mainly on particle thickness and size. The standard deviations were <30% for Na, K, and Ca, <10–15% for Al and Mg, and <5% for Si and Fe, equivalent to an analytical error of <2 wt.% for most of the major elements. Structural formulae were calculated on the basis of 22 negative charges, according to Bailey *et al.* (1980), assuming (1) the iron present is ferric Fe, (2) the tetrahedral $Si^{4+}$ + $Al^{3+}$ is equal to 4, (3) $Fe^{3+}$, $Mg^{2+}$, and $Al^{3+}_{rest}$ occupying the octahedral sheet, and (4) $K^+$, $Na^+$, and $Ca^{2+}$ are located within the interlayer sites.

*Focused-ion beam and scanning electron microscope (FIB-SEM) study*

The microfabrics of light and dark green clay infillings of the benthic foraminifer *Fursenkoina mexicana* were studied using a Zeiss Auriga CrossBeam FIB-SEM (Oberkochen, Germany). A Pt-coated surface area of ~20 μm × 30 μm was tilted normal to the ion beam. Ion milling was applied to create a cross-sectional surface of ~15 μm × 15 μm that was imaged by the electron beam with a 5 kV accelerating voltage. 3-D information was obtained using a serial sectioning procedure with alternating milling and imaging to acquire a 2-D image sequence across the selected volume (Warr and Grathoff, 2012). The acquired number of secondary electron images ranged between 100 and 300 with a 25 nm slice thickness. 3-D visualization was obtained from the sequence of SEM images using *ImageJ*© (developed by W. Rasband, National Institutes of Health) based on the gray-level contrasts. The distribution of clay matter, pore space, and skeletal calcite was reconstructed using a threshold method slightly modified from that described by Keller *et al.* (2011).

## RESULTS

In this section, the results of petrographic, mineralogical, geochemical, and structural studies of the bulk sediment and the green grains are compared in order to investigate the glauconitization process in the recent deep-sea environment of the ODP Site 959C.

*Petrographic observations*

The uppermost 25 m of sediment consists of slightly bioturbated, olive brown to olive-grayish green horizons of interbedded foraminifera and nanofossil oozes. The laminae which are rich in foraminifera tests are ~1 mm to 1 cm thick and show two scour contacts at ~3.8 and 10.4 mbsf. Giresse *et al.* (1998) interpreted these as resulting from winnowing action or longer breaks in sedimentation. Darker intervals are rich in organic matter (0.7–1.6 wt.%) with a C/N ratio of 8–48 (14 on average), as reported by Baldermann (2012), which indicates the predominance of marine organic matter (Wagner, 1998). These thinner layers also contain large proportions of coccoliths which are mixed with a brownish clay matrix. Sparse occurrences of large detrital quartz and feldspar grains as well as plant debris were recognized over the whole sedimentary sequence whereas the proportions of pyrite and green clay infillings related to glauconitization increase slightly with increasing depth (Baldermann, 2012). No signs of gravity-flow or turbidity deposits are evident, indicating that the green grains were formed *in situ* rather than transported by reworking and re-deposition from the surrounding Ghanaian shelf and slope.

Examples of microfacies and microstructures from 1.32, 10.23, 11.49, and 24.91 mbsf (see Figure 2) reveal that the sediment from 1.32 mbsf consists of nanofossil ooze which is rich in the tests of globigerine and orbuline foraminifera that show a few incomplete, pale to light green clay infillings in addition to some radiolarians (Figure 2a). No pyrite was found, suggesting that the uppermost sediments are the least altered in terms of diagenetic overprinting. At 10.23 mbsf, foraminifera tests mixed with partly dissolved radiolarians dominate in the sediment and some of these tests show immature, light to medium green clay infillings (Figure 2b). Many medium green internal moulds and subordinate pyrite infillings were found within the foraminifera tests at 11.49 mbsf (Figure 2c). Radiolarians are largely absent at ⩾11.49 mbsf, and skeletal calcite (foraminifera tests) has been partly dissolved. Abundant more-mature, medium to dark green grains with a fractured and broken morphology, and many pyrite infillings, were found at 24.91 mbsf (Figure 2d). The section ⩾24.91 mbsf is, thus, considered to reflect the most altered sediment with respect to early diagenesis. An increased state of glauconitization is recognizable in the more deeply buried sediments, together with precipitation of pyrite and dissolution of both carbonate and bio-opal.

*Bulk mineralogy of Hole 959C*

Quantitative XRD analyses of 21 bulk samples from Hole 959C (see Figure 3) revealed a relatively constant background of siliciclastic input during the last 2.5 My, consisting of poorly crystalline kaolinite (21–34 wt.%), quartz (11–19 wt.%), and feldspar (3–8 wt.% of K-feldspar and albite), and minor proportions of detrital smectite (2–5 wt.%), illite/muscovite (1–5 wt.%), chlorite (1–3 wt.%), and anatase (0.3–0.6 wt.%). In addition to the detrital input, authigenic calcite (27–51 wt.%), Gl-S (1–6 wt.% with an average of 2–3 wt.%), and pyrite (<3 wt.%) were formed. Traces (<1 wt.%) of aragonite, bio-opal, and Fe-(oxyhydr)-oxides as well as secondary halite, gypsum, and hexahydrite were also identified by SEM, most of

https://doi.org/10.1346/CCMN.2013.0610307 Published online by Cambridge University Press

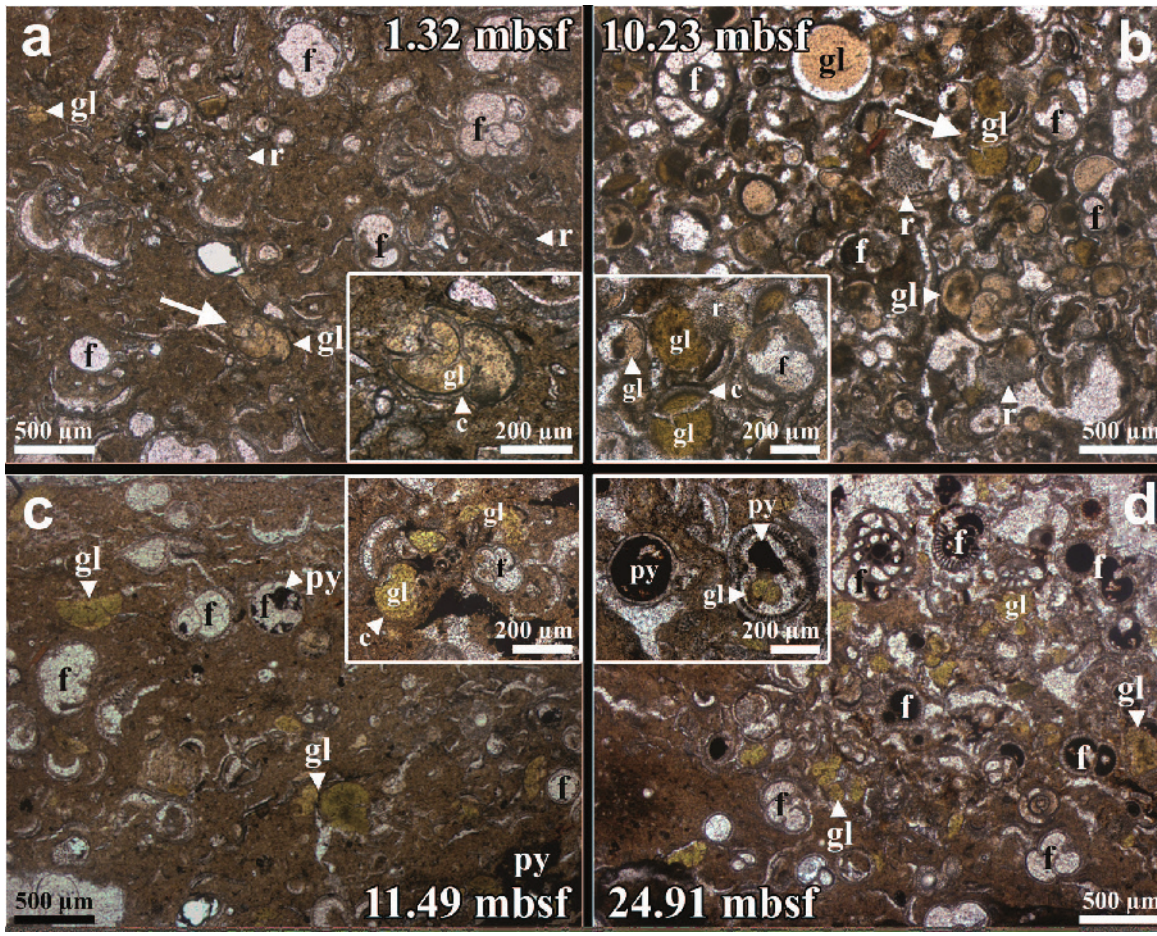


Figure 2. Photomicrographs showing the development of microfacies and microstructure within the upper 25 m of Hole 959C. (a) Clayey nanofossil ooze enriched in foraminifera (f) and radiolarians (r) from 1.32 mbsf. Incomplete, light green clay infillings (gl) are scarce. (b) Immature, light to medium green clay infillings in foraminifera ooze mixed with partly dissolved radiolarians from 10.23 mbsf. (c) Nanofossil ooze containing interbedded laminae of foraminifera tests rich in medium green clay and subordinate pyrite infillings (py). Radiolarians are largely absent at 11.49 mbsf and skeletal calcite (c) is partly dissolved. (d) Foraminifera-rich nanofossil ooze with large proportions of more mature dark green grains showing a modified (broken or cracked) morphology accompanying plentiful pyrite infillings from 24.91 mbsf.

which probably formed as alteration products during storage at the Bremen Core Repository. No general variation with depth in the basic mineral assemblage was detected except an increase in the amount of pyrite (and Gl-S) and a decrease in the proportion of feldspar with increasing depth which can be attributed to diagenetic alterations (Figure 3).

Observations by SEM of carbonate-free sediment from 0.16 mbsf showed it to have slightly rounded quartz grains, in addition to detrital K-feldspar, albite, chlorite, and illite/muscovite particles that show clear cleavage directions and distinct crystal edges with no signs of diagenetic modification (Figure 4). Modified habits, abundant dissolution pits, and decomposition features are evident at 24.91 mbsf, indicating silicate alterations related to progressing marine diagenesis. Fe-(oxyhydr)oxides and unstable bio-opal (fragments of radiolarians, diatoms, and sponge needles) have been almost completely dissolved or have been partly glauconitized at 24.91 mbsf, whereas detrital smectite and kaolinite remained unaltered (Figure 4). Neo-crystallized pyrite with both framboidal and euhedral (octahedral) morphology is most abundant at 24.91 mbsf, together with authigenic Gl-S.

*Mineralogy of the green-grain sub-fractions*

The material inside the foraminifera shells, namely the green clay infillings, was studied by XRD after removal of the skeletal carbonate and surrounding mud matrix. In order to investigate the state of glauconitization in the more deeply buried sediments, clay matter from the pale to light green, medium green, and dark green-grain sub-fractions from 0.16, 11.69, and 24.91 mbsf was analyzed using oriented clay preparations (Figure 5). Air-dried clay from the light green grains from 0.16 mbsf displayed a $d_{001}$ reflection at

https://doi.org/10.1346/CCMN.2013.0610307 Published online by Cambridge University Press

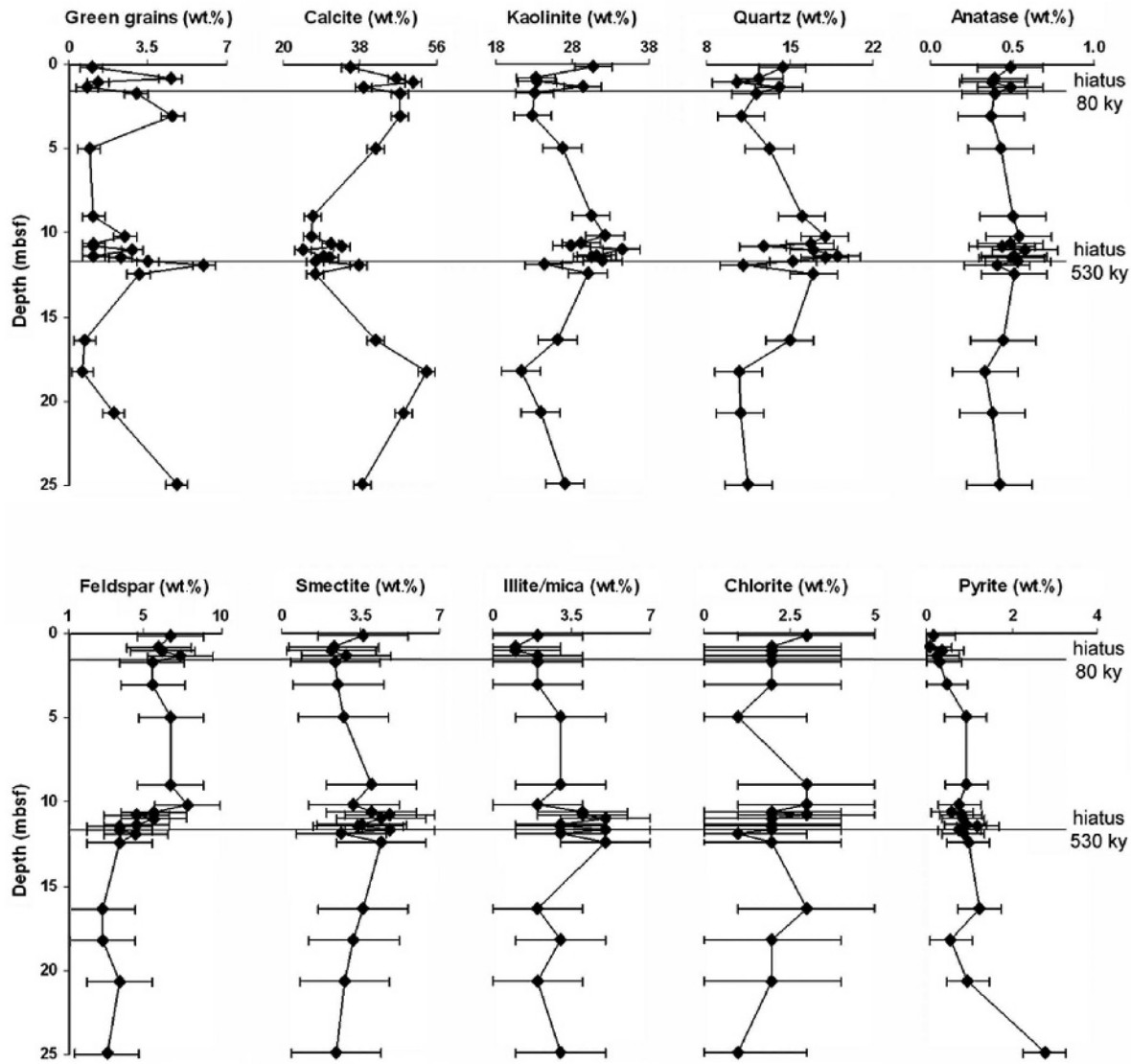


Figure 3. Bulk mineralogy of the upper 25 m of Hole 959C based on XRD. The proportion of the green-grain fractions was determined by weighing.

13.3 Å which shifted to 16.5 Å after EG-solvation with the weak $d_{002}$ reflection at 8.8 Å, typical for immature Fe-smectite-rich Gl-S. In contrast, air-dried clay matter from the buried, dark green grains from 24.91 mbsf showed a $d_{001}$ value at 11.4 Å which increased to 14.8 Å after EG solvation. The $d_{002}$ value was 9.7 Å, indicative of a more mature glauconite-rich Gl-S. After heating to 550ºC for 1 h the basal spacing decreased to 10.0 Å.

Quantitative changes in both the composition of Gl-S and the percentage of each green-grain sub-fraction suggest a sequence of increased glauconitization with increasing burial depth (Figure 5). Using the linear relationship between the %Gl in Gl-S and related shifts in their basal spacings (adapted from Moore and Reynolds, 1997), the $d_{002}$ reflections from EG-solvated clay matter were used to determine the %Gl in each green-grain sub-fraction (Figure 5). *Sybilla*© modeling (Figure 5) of the XRD patterns reveals that the most immature Gl-S from 0.16 mbsf contains ~32% Gl and ~68% Fe-smectite layers (R0 ordered), whereas the most mature Gl-S from 24.91 mbsf contains ~84% Gl and ~16% Fe-smectite layers (R3 ordered). These values are consistent with the %Gl values obtained by using the Moore and Reynolds method. The %Gl increased, together with greening of the grain color, from 32–51% (light green) and 39–74% (medium green) to 61–84% (dark green). The mass fraction (determined by weighing) of the light green grains in the total green-grain fraction decreases with increasing depth, from 70 wt.% at 0.16 mbsf to 20 wt.% at 11.69 mbsf and to 5 wt.% at 24.91 mbsf. Correspondingly, the mass fractions of medium (30 wt.%, 50 wt.%, and 55 wt.%)

https://doi.org/10.1346/CCMN.2013.0610307 Published online by Cambridge University Press

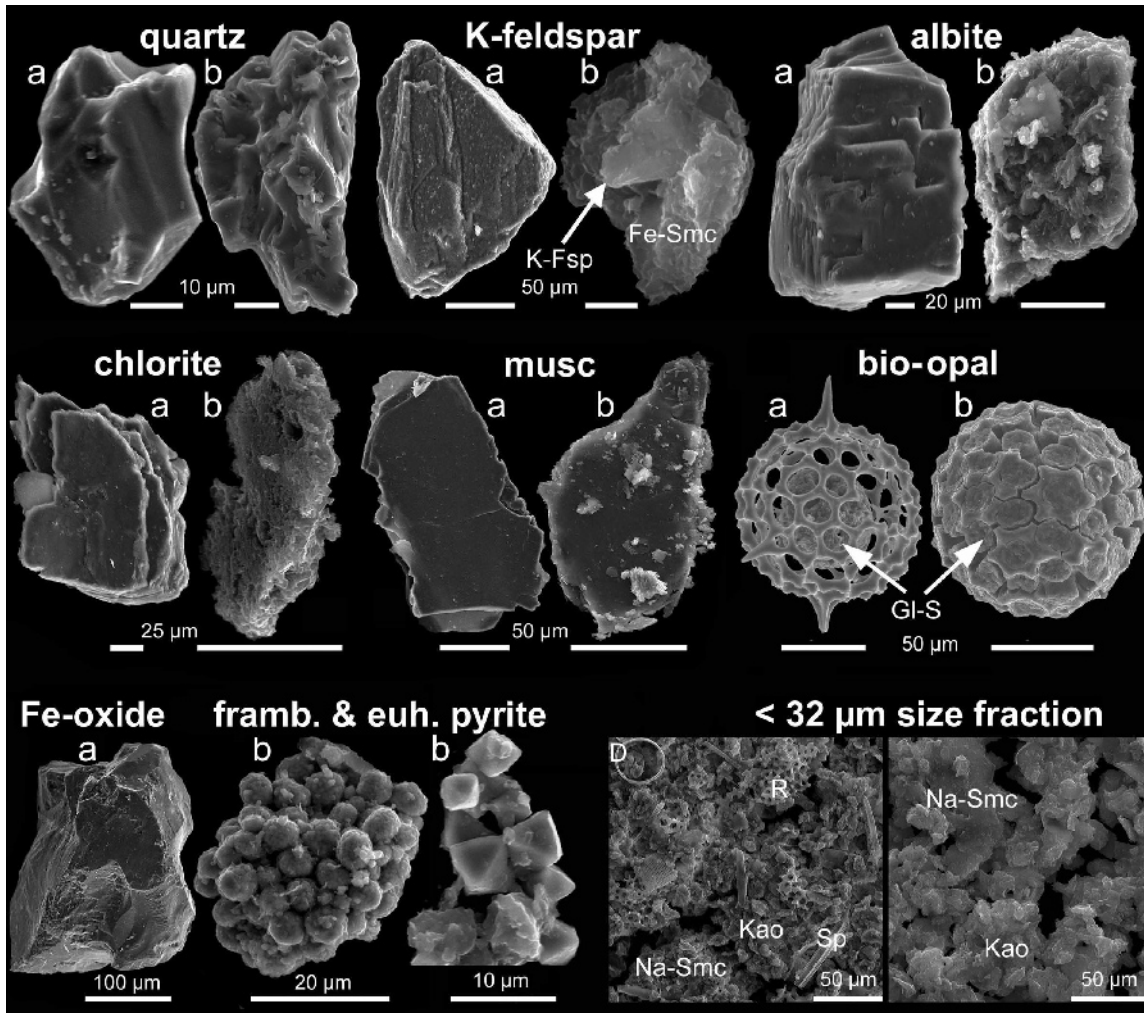


Figure 4. SEM images of less altered selected grains from 0.16 mbsf (a) compared with the more altered grains from 24.91 mbsf (b). Quartz, K-feldspar, albite, chlorite, muscovite (musc), bio-opal (Sp = sponge needles, D = diatoms, R = radiolarians), and Fe-(oxyhydr)oxide show abundant alteration and dissolution features, while detrital Na-smectite (Na-Smc) and kaolinite (Kao) remain unaltered. Glauconite-smectite (Gl-S) and framboidal and euhedral pyrite (framb. and euh. pyrite) were formed *in situ* during early marine diagenesis.

and dark green grains (<5 wt.%, 30 wt.%, and 40 wt.%) increased at the three depths (Figure 5). In each grain color class the %Gl increased with increasing depth, from 32–39% at 0.16 mbsf and 36–61% at 11.69 mbsf to 51–84% at 24.91 mbsf, attributed to ongoing glauconitization related to progressive diagenesis. All %Gl values were notably greater than the value reported by Wiewióra *et al.* (2001) who estimated only ~20% Gl layers for the green-grain assemblages without separation of the light, medium, and dark sub-fractions.

*Composition, form, and structure of clay minerals in the green-grain sub-fractions*

The composition, form, and structure of clay-mineral particles from the separated light, medium, and dark green-grain sub-fractions from 0.16, 11.69, and 24.91 mbsf of Hole 959C were studied by TEM-EDX and TEM-SAED in order to identify differences attributed to variations in these properties related to burial depth and color of the green clays (Figure 6, Table 1). In total, 332 TEM-EDX analyses were carried out on single clay-mineral particles and structural formulae were calculated, based on average compositions. Nine TEM-EDX analyses were also carried out on biofilm (see below).

Particles of the light green sub-fractions generally have a veil-like or film morphology according to the nomenclature of Buatier *et al.* (1989). These particles consist mainly of Fe-smectites and smectite-rich Gl-S that predominantly display weak diffraction rings reflecting their turbostratic nature (Figure 6a,d,g). Bacteria are frequently present within the light green sub-fractions but they are less abundant in the darker, more mature grains. In close proximity to bacteria,

https://doi.org/10.1346/CCMN.2013.0610307 Published online by Cambridge University Press

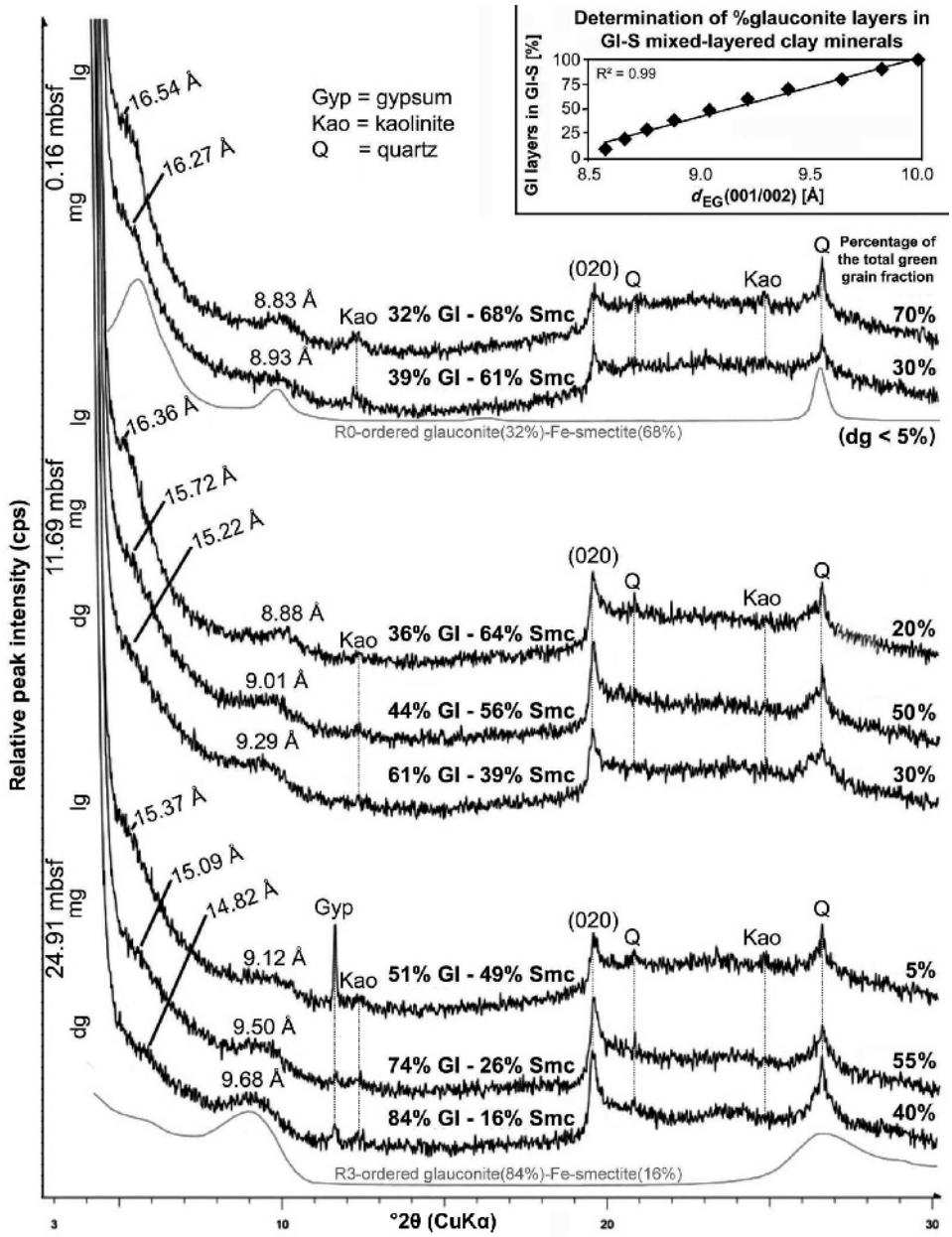


Figure 5. XRD patterns of oriented, glycolated preparations of the separated light (lg), medium (mg), and dark green (dg) grains, collected from 0.16, 11.69, and 24.91 mbsf of Hole 959C. The %Gl in Gl-S was calculated using the linear equation %Gl = 60.8 · $d_{EG}002 - 504.5$ derived from *NEWMOD*-calculated %illite in illite-smectite *vs.* $d_{EG}002$ peak-position relations reported by Moore and Reynolds (1997). The accuracy of the %Gl estimations was verified by comparison with *Sybilla* calculations (gray curves). On the right, the percentage of each green-grain sub-fraction is given in wt.% of the total green-grain fraction (determined by weighing).

biofilm is often mixed with thin Fe-smectite particles, suggestive of bacteria–clay mineral interactions. Intermediate Gl-S particles with both flaky and lath-like morphology occur rarely at 0.16 mbsf but their abundance increases with increasing depth along with greening of the grain color (Figure 6b,e,g,h). Accordingly, minor proportions of Fe-smectite-rich Gl-S with either smeared Bragg spots or unsharp diffraction rings still occur at 11.69 and 24.91 mbsf but lath-like, glauconite-rich Gl-S with discrete Bragg spots predominate. Within the dark green sub-fractions, intermediate and lath-like glauconite particles as well as flake-shaped, glauconite-rich Gl-S are more frequent. The elongated form of these particle types (Figure 6c,f,h, and in the lower right of panel i) is evident from the high aspect ratio of 4:1 to 5:1. Such more evolved, lath-like particles commonly display discrete Bragg spots, documenting a more ordered mineral structure (*e.g.*

https://doi.org/10.1346/CCMN.2013.0610307 Published online by Cambridge University Press

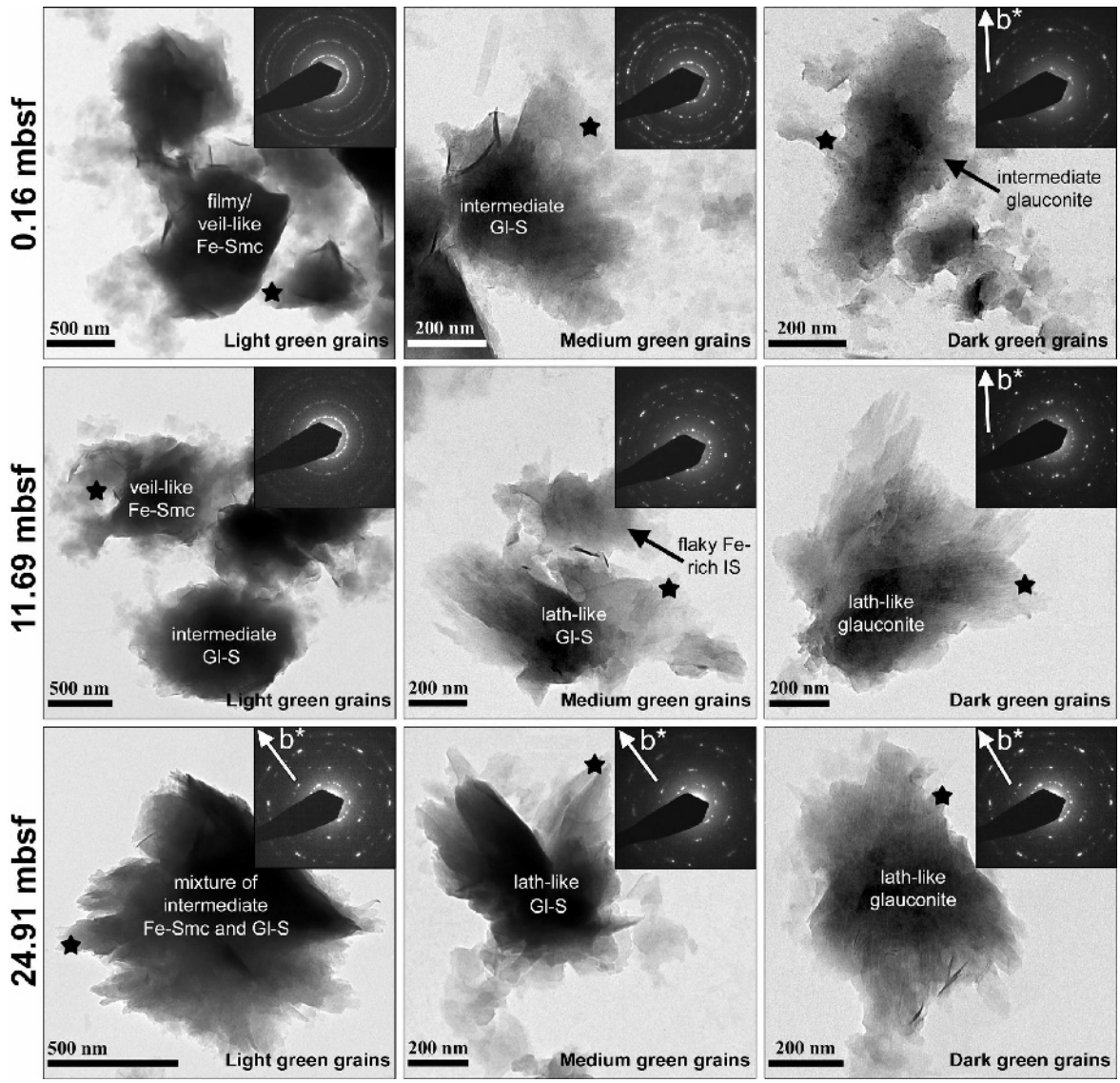


Figure 6. TEM images and TEM-SAED patterns of representative clay mineral particles from the light, medium, and dark green-grain sub-fractions from 0.16 (a–c), 11.69 (d–f), and 24.91 mbsf (g–i) showing the development of particle form and composition at Hole 959C. Initial filmy or veil-like Fe-smectite (Fe-Smc) (a,d) with weak diffraction rings changes into intermediate, flaky, or lath-like Gl-S (b,e,g,h) with weak or smeared Bragg spots and finally into lath-like glauconite (c,f,i). The two diagnostic, non-basal Bragg reflections (b* marks the direction of the *b* axis) indicate a transition from the poorly ordered 1*M*d-polytype to the ordered 1*M*-polytype.

Baldermann *et al.*, 2012) compared to that of Fe-smectite.

According to the chemical composition (based on TEM-EDX analysis), the clay-mineral particles mainly consist of Si, Fe, Al, Mg, K, Ca, and O with small traces of P, S, Ti, and Mn (Table 1). With increasing maturity of the grains, the following changes in elemental chemistry were recognized. Average compositions of the light green clay-mineral particles were rather poor in $K_2O$ (1.8–2.9 wt.%), MgO (3.8–4.4 wt.%), and $Fe_2O_3$ (24.7–25.2 wt.%), whereas $SiO_2$ (60.0–61.1 wt.%), $Al_2O_3$ (7.1–7.6 wt.%), and CaO (0.4–0.8 wt.%) proportions were high. The medium green clay-mineral particles have moderate amounts of $K_2O$ (2.6–4.3 wt.%), MgO (3.7–4.4 wt.%), CaO (0.4–0.8 wt.%), and $Fe_2O_3$ (25.0–26.0 wt.%), but less $SiO_2$ (58.8–61.1 wt.%) and $Al_2O_3$ (6.5–7.1 wt.%). Finally, the dark green clay-mineral particles have the largest amount of $K_2O$ (4.3–5.4 wt.%) and $Fe_2O_3$ (24.0–27.3 wt.%), moderate MgO (4.2 wt.%) and CaO (0.4–0.8 wt.%), but the smallest amount of $SiO_2$ (58.2–59.1 wt.%) and $Al_2O_3$ (5.2–7.3 wt.%). Based on

https://doi.org/10.1346/CCMN.2013.0610307 Published online by Cambridge University Press

Table 1. Averaged compositions, excluding water of Gl-S, based on 332 TEM-EDX analyses, with calculated structural formulae of the separated light, medium, and dark green-grain sub-fractions from samples taken at 0.16, 11.69, and 24.91 mbsf.

| Depth | —— 0.16 mbsf —— | | | —— 11.69 mbsf —— | | | —— 24.91 mbsf —— | | |
|---|---|---|---|---|---|---|---|---|---|
| Green-grain sub-fraction | light | medium | dark | light | medium | dark | light | medium | dark |
| Particles analyzed (*n*) | 32 | 36 | 30 | 36 | 34 | 38 | 39 | 43 | 44 |
| Averaged elemental chemistry (wt.%) based on TEM-EDX | | | | | | | | | |
| MgO | 4.0 | 3.7 | 4.2 | 3.8 | 4.1 | 4.2 | 4.4 | 4.4 | 4.2 |
| $Al_2O_3$ | 7.6 | 7.1 | 7.3 | 7.5 | 6.5 | 5.2 | 7.1 | 6.1 | 5.2 |
| $SiO_2$ | 61.1 | 61.1 | 59.1 | 61.2 | 59.8 | 58.5 | 60.0 | 58.8 | 58.2 |
| $K_2O$ | 2.2 | 2.6 | 4.6 | 1.8 | 3.1 | 4.3 | 2.9 | 4.3 | 5.4 |
| $Fe_2O_3$ | 24.7 | 25.0 | 24.0 | 24.8 | 25.7 | 27.3 | 25.2 | 26.0 | 26.7 |
| CaO | 0.4 | 0.5 | 0.8 | 0.8 | 0.8 | 0.4 | 0.5 | 0.4 | 0.4 |
| Total | 100.0 | 100.0 | 100.0 | 100.0 | 100.0 | 100.0 | 100.0 | 100.0 | 100.0 |
| Atoms per formula unit (a.p.f.u.) based on $O_{10}(OH)_2$ | | | | | | | | | |
| $^{IV}Al$ | 0.08 | 0.06 | 0.14 | 0.07 | 0.11 | 0.14 | 0.12 | 0.14 | 0.14 |
| Si | 3.92 | 3.94 | 3.86 | 3.93 | 3.89 | 3.86 | 3.88 | 3.86 | 3.86 |
| TC | −0.08 | −0.06 | −0.14 | −0.07 | −0.11 | −0.14 | −0.12 | −0.14 | −0.14 |
| $^{VI}Al$ | 0.50 | 0.48 | 0.43 | 0.49 | 0.39 | 0.27 | 0.43 | 0.33 | 0.26 |
| Fe (III) | 1.19 | 1.21 | 1.18 | 1.20 | 1.26 | 1.36 | 1.23 | 1.28 | 1.33 |
| Mg | 0.38 | 0.36 | 0.41 | 0.37 | 0.39 | 0.42 | 0.42 | 0.43 | 0.42 |
| $\Sigma(^{VI}Al + Fe (III) + Mg)$ | 2.07 | 2.05 | 2.02 | 2.06 | 2.04 | 2.05 | 2.08 | 2.04 | 2.01 |
| OC | −0.17 | −0.21 | −0.35 | −0.19 | −0.27 | −0.27 | −0.18 | −0.31 | −0.39 |
| K | 0.18 | 0.21 | 0.38 | 0.15 | 0.26 | 0.36 | 0.24 | 0.36 | 0.46 |
| Ca | 0.03 | 0.03 | 0.05 | 0.06 | 0.06 | 0.03 | 0.03 | 0.04 | 0.03 |
| IC | 0.24 | 0.27 | 0.48 | 0.27 | 0.38 | 0.42 | 0.30 | 0.44 | 0.52 |

TC = tetrahedral charge, OC = octahedral charge, IC = interlayer charge.

the calculated, average structural formulae (Table 1), the light green clay-mineral particles have an Fe-smectite composition of $(K_{0.18}Ca_{0.03})(Fe^{3+}_{1.19}Al_{0.50}Mg_{0.38})_{\Sigma 2.07}[Al_{0.08}Si_{3.92}O_{10}](OH)_2$ at 0.16 mbsf. Gl-S compositions of $(K_{0.26}Ca_{0.06})(Fe^{3+}_{1.26}Al_{0.39}Mg_{0.39})_{\Sigma 2.04}[Al_{0.11}Si_{3.89}O_{10}](OH)_2$ dominate in the medium green grains from 11.69 mbsf, whereas the most mature, dark green glauconite-rich Gl-S have compositions of $(K_{0.46}Ca_{0.03})(Fe^{3+}_{1.33}Al_{0.26}Mg_{0.42})_{\Sigma 2.01}[Al_{0.14}Si_{3.86}O_{10}](OH)_2$ at 24.91 mbsf. Due to the high Fe-smectite content, especially in the less evolved Gl-S, some of the $Mg^{2+}$ may be located in the interlayer sites of the Fe-smectite which could increase the interlayer charge of Gl-S by a progressively higher octahedral charge deficiency. The greener color of the more mature grains may also reflect the existence of some structural $Fe^{2+}$ which could affect the structural formulae by decreasing the tetrahedral Si content. However, the $Fe^{2+}/Fe^{3+}$ ratio in glauconite is commonly rather low, typically ranging from 0.05 to 0.5 at most (~0.15 is the average, inferred from the data reported by Meunier and El Albani, 2007), and the calculated structural formulae are balanced assuming the Fe is ferric (Table 1). The overall compositional changes mentioned above, thus, support a sequence of increased glauconitization with increasing burial depth, whereby initial Fe-smectites changed continuously into glauconite *via* the formation of Gl-S, as also indicated by the XRD data (Figure 5).

### *3-D microstructure of light vs. dark green clay infillings*

Differences of microstructure, microporosity, and mineralogy between the light and dark green clays were studied by comparison of 3-D reconstructions of infillings in the benthic foraminifer *Fursenkoina mexicana* (Figure 7). At 0.16 mbsf, most of these shells are filled with light green clay matter but at 24.91 mbsf most are filled with dark green clay matter. One shell filled with light green clay matter and one filled with dark green clay matter were selected for the study. The following observations were made on the two varieties:

(1) The light green clay matter from 0.16 mbsf (Figure 7a–c) consisted mainly of sets of Fe-smectite-rich Gl-S ~0.5–1.0 μm across and subordinate Fe-smectite particles. These poorly evolved clay minerals (nomenclature of Odin and Matter, 1981) typically form boxwork-like networks (Figure 7b) with a significant, well connected porosity of ~15–20% (Figure 7c). Fragments of partly dissolved calcite (Figure 7a) which are probably remnants of the foraminifera walls are well preserved between the clayey frameworks.

https://doi.org/10.1346/CCMN.2013.0610307 Published online by Cambridge University Press

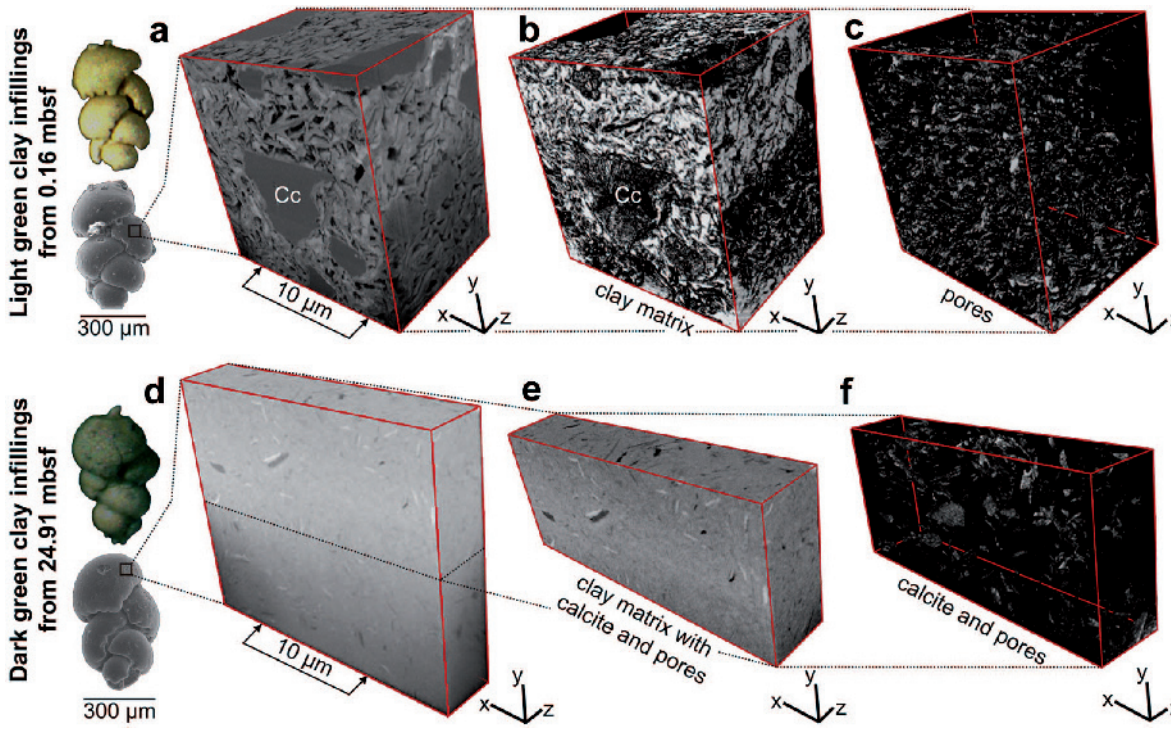


Figure 7. 3-D reconstructions of green clay infillings of the benthic foraminifera, *Fursenkoina mexicana*, based on FIB-SEM images. Optical photomicrographs and SE images of the specimens, filled with either light green clay at 0.16 mbsf (a) or dark green clay at 24.91 mbsf (d), show the locations of the investigated areas. The light green clay matter (a–c) is composed mainly of 0.5–1 µm long Fe-smectite-rich Gl-S (white areas in part b) which forms boxwork-like networks with a high porosity (white areas in part c). Skeletal calcite (dark gray areas in part a marked with Cc) is largely preserved. The dark green clay matter (d–e) is composed of sets of 0.5–2 µm long glauconite-rich Gl-S (gray areas in part e) and forms rosette-like structures with a greater packing density. Pore space and skeletal calcite (white areas in part f) are largely reduced at this state of glauconitization.

(2) The dark green clay matter from 24.91 mbsf (Figure 7d–f) consisted mainly of glauconite-rich Gl-S and showed more complex microstructures than those of the light green clays. Sets of these clay-mineral particles are ~0.5–2.0 µm in size and typically form flame- or rosette-like structures with a high packing density (Figure 7d,e), characteristics associated with the evolved state of glauconitization (Odin and Matter, 1981). At this state, the porosity (5–10%) is reduced and the skeletal calcite has largely been dissolved (Figure 7f). Such (micro)-textures indicate changes in the physicochemical conditions in the foraminifera tests during progressive glauconitization.

## DISCUSSION

Previous studies demonstrated that in the deep-water environment of the Ivory Coast–Ghana Marginal Ridge (ODP Hole 959C), authigenic green clay minerals initially formed at the water–sediment interface during phases of enhanced ion exchange with the seawater (Giresse and Wiewióra, 2001; Wiewióra *et al.*, 2001). The reaction mechanism proposed was that of Fe-smectite-to-glauconite alteration by the formation of Gl-S, a feature confirmed in the present study. However, detailed XRD and electron microscope analyses of representative green grains from different depths revealed a number of new features which were not characterized by previous authors: (1) the association of biofilm, gels, and co-precipitated Fe-smectite in less altered grains; (2) the decrease in connected porosity with increasing depth; (3) a greater abundance of glauconite in Gl-S in all samples; and (4) a notable depth-dependent increase in the degree of glauconitization which was observed for all three types of green grains – light, medium, and dark – together with increasing proportions of the dark green grains with increasing burial depth. In this section, the key factors for glauconitization are discussed and a new interpretation of glauconite formation presented. The availability of Fe is suggested to be the most important rate-limiting factor for the glauconitization process in this low-temperature, deep-water setting.

### *The initial step to glauconitization – formation of Fe-smectite*

Comparison of petrographic (Figure 2), mineralogical (Figure 5), and chemical (Table 1) data across the entire range of green clay minerals from the immature light green grains from 0.16 mbsf to the most mature dark

https://doi.org/10.1346/CCMN.2013.0610307 Published online by Cambridge University Press

green grains from 24.91 mbsf suggests that a complete, genetically related mineral series from initial Fe-smectite to glauconite exists *via* progressively more glauconitic Gl-S. Thus, the early diagenetic formation of Fe-smectite subsequent to sediment deposition seems to be a key factor for glauconitization of foraminifera tests, as proposed by Giresse and Wiewióra (2001).

Authigenic veil-like Fe-smectite particles ~20–50 nm long are always associated with bacteria-produced biofilm (Figure 8a,b). The biofilm contains, on average, high proportions of volatiles (89.1 wt.% $CO_2$ and 1.9 wt.% $SO_3$) and $SiO_2$ (4.6 wt.%), CaO (1.8 wt.%), $P_2O_5$ (1.6 wt.%), $Fe_2O_3$ (0.4 wt.%), MgO (0.4 wt.%), and $K_2O$ (0.1 wt.%) based on nine TEM-EDX analyses (Figure 8). Such a composition is indicative of bacterial biofilm of marine origin with incorporated amorphous gels, rather than that resulting from later contamination, with similarities to biofilm compositions produced in experimental studies of seawater, clay mineral, biofilm, and bacteria interactions (*e.g.* Chaerun and Tazaki, 2005; Warr *et al.*, 2009). According to Konhauser and Urrutia (1999), a Si-rich precursor gel is suggested to promote clay-mineral authigenesis. Smectite precipitation from amorphous gels was proposed previously by Harder (1980), Jiménez-Millán *et al.* (1998), Kloprogge *et al.* (1999), and Gaudin *et al.* (2005). The biofilm can provide an early micro-environment where suitable conditions for the formation of amorphous $Fe^{3+}/Mg^{2+}$-rich hydrogel with co-precipitated $Al^{3+}$ develop as soon as supersaturation is reached (Konhauser and Urrutia, 1999). Rapid chemisorption of dissolved silica onto this initial precipitate (Martín-Algarra and Sánchez-Navas, 1995) can finally lead to the development of poorly crystalline Fe-smectite-like phases, as found in the surface sediments of ODP Site 959 (Figures 8b, 9). These largely unaltered Fe-smectite particles contain ~8% Gl and ~92% Fe-smectite layers and can be classified as the nascent state of glauconitization (nomenclature of Odin and Fullagar, 1988). The early micro-environment developed within the bacterial biofilm is, therefore, suitable for Fe-smectite formation which is likely to be the first step of the glauconitization process within the Ivory Coast sediments (Figure 9).

With the increased state of glauconitization found in the more deeply buried sediments, the proportion of bacteria present within the internal moulds of the calcareous (pelagic) foraminifera decreased notably, probably reflecting the intense changes in pH and Eh conditions within the micro-environment. As the microbial activity decreases, the interstitial solution of the bulk sediment and its chemistry are expected to become more important and control the ongoing glauconitization

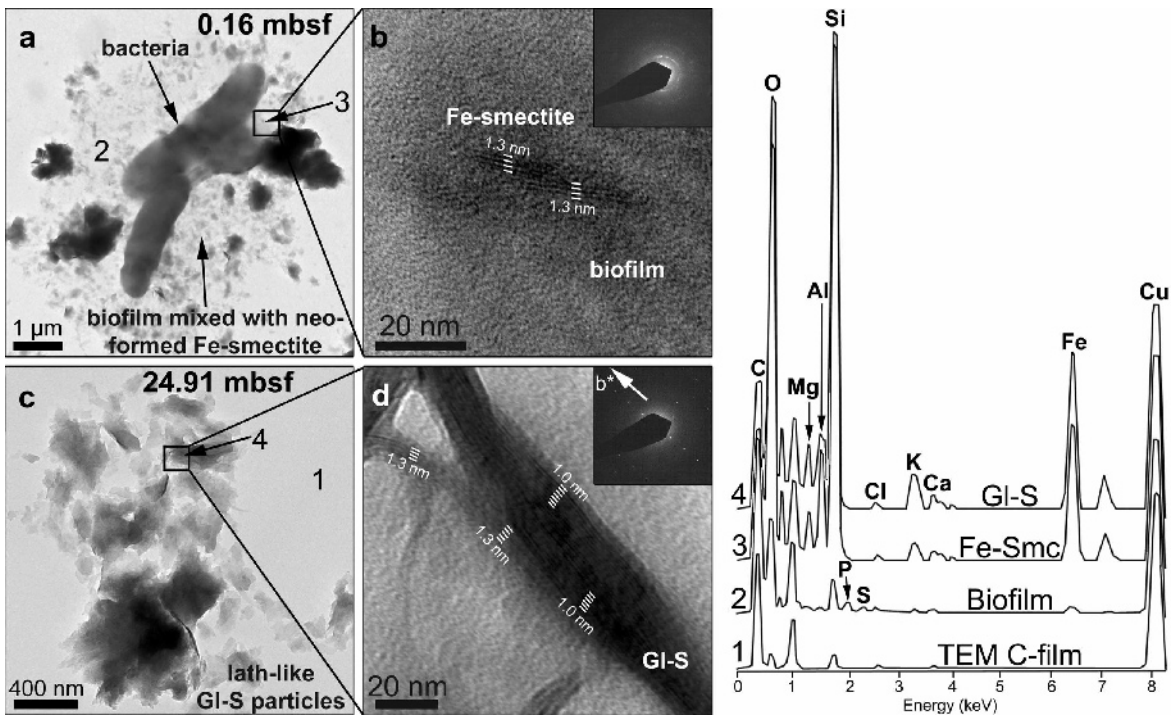


Figure 8. TEM images illustrating the evolution of the green clay minerals at ODP Site 959. (a) Interactions of authigenic Fe-smectites and bacterial biofilm from 0.16 mbsf. (b) An enlarged view of (a) which shows the association of neo-formed Fe-smectite-like phases and biofilm. (c–d) Lath-like Gl-S particles without bacteria from 24.91 mbsf indicative of an ongoing glauconitization process. On the right, TEM-EDX spectra of TEM C-film (1), biofilm mixed with neo-formed Fe-smectite (2), pure Fe-smectite (3), and Gl-S (4) are shown.

https://doi.org/10.1346/CCMN.2013.0610307 Published online by Cambridge University Press

process. This interstitial solution-driven Fe-smectite-to-glauconite reaction is evident from the greater degree of glauconitization observed at 24.91 mbsf (Figure 8c,d).

*The driving force for glauconitization – interstitial solution chemistry*

Recent green-clay authigenesis is commonly restricted to granular siliciclastic and calcareous habitats. The original composition of the sediment and the residence time close to the sediment–seawater interface (Giresse and Wiewióra, 2001) are thought to be the key factors controlling the glauconitization reaction. Such conditions imply continuous cation supply solely from seawater during the whole glauconitization process. Effective cation exchange can only take place in the first centimeters of clayey substrates and in the first meters of granular substrates, depending on the properties of the sediment such as permeability, porosity, tortuosity, and mainly on the sedimentation rate (Meunier and El Albani, 2007). At Hole 959C, the sediment's properties (Mascle *et al.*, 1996) and sedimentation rates (Wagner, 1998) have not changed noticeably over the last 2.5 My, whereas XRD, TEM-EDX, and FIB-SEM data from the present study clearly reveal an increasing state of glauconitization with increasing depth (Figures 6, 9), thus indicating that the glauconitization reaction is not restricted to the seafloor–sediment interface and proceeds further during progressive burial. Furthermore, if the Fe-smectite precursors were precipitated solely from seawater, then an explanation is required for why the mineralogy (Figure 5) and the chemistry of the green grains differ (Table 1), despite a similar residence time close to the sediment–seawater interface at this site (~1 cm/ky) characterized by constant cation supply. These relationships may be explained by the interstitial solution chemistry being modified by microbially catalyzed oxidation of biodegradable (marine) organic matter, causing Fe redox reactions and silicate alterations (Figures 2–4) that promoted the ongoing glauconitization process within the sediment pile.

Microbial oxidation of marine organic matter was suggested by Mascle *et al.* (1996) to have had a major impact on the diagenetic reactions observed at Site 959, namely glauconitization and pyritization. Within the first few meters of sediments, the $SO_4^{2-}$ concentration of the interstitial solution drops below the level of the seawater, owing to microbial sulfate reduction. Thus, dissolved oxygen has been consumed quantitatively (Schulz and Zabel, 2006), followed by $Mn^{4+}$ and $Fe^{3+}$ reduction (Figure 10), *e.g.* from (oxyhydr)oxides. Accompanying ongoing $SO_4^{2-}$ reduction with increasing depth, $H_2S$ accumulated successively in the interstitial solution, providing the anions for framboidal and euhedral pyrite formation (Figures 3, 4). Fe-sulfide precipitation is, thus, a limiting factor for glauconitization because it competes with the primary formation of Fe-smectites by removal of ferrous Fe. As a consequence, the Fe interstitial solution profile displays large variation in Fe content without any systematic depth

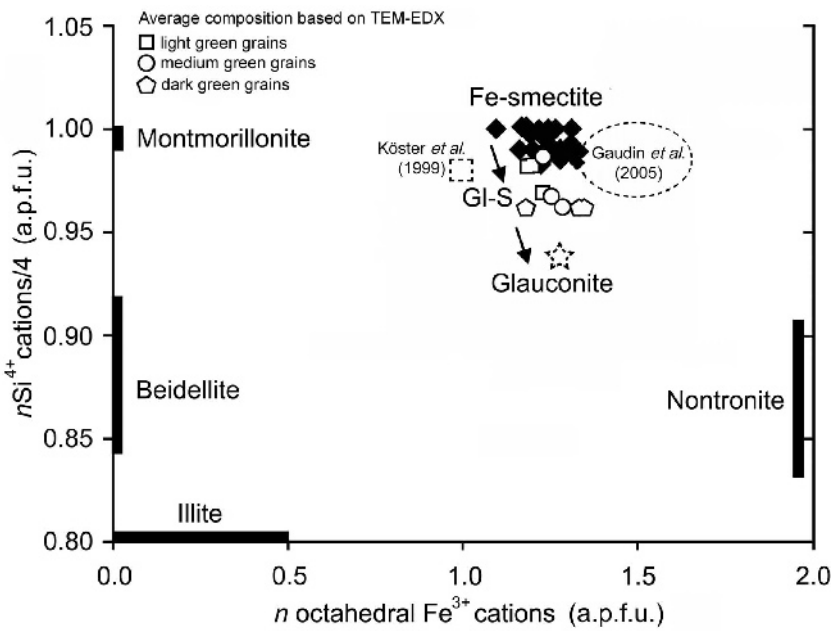


Figure 9. TEM-EDX analyses of unaltered Fe-smectite particles from 0.16 mbsf of Hole 959C (black rhombs) plotted in the $^{4}Si-\Sigma^{VI}Fe$ diagram of Gaudin *et al.* (2005). Average compositions of the separated green-grain sub-fractions (Table 1) are included to illustrate the ongoing glauconitization process. Reference data of Fe-smectite (dashed circle and square) and of the international GLO (glauconite) standard (dashed star) are included for comparison.

https://doi.org/10.1346/CCMN.2013.0610307 Published online by Cambridge University Press

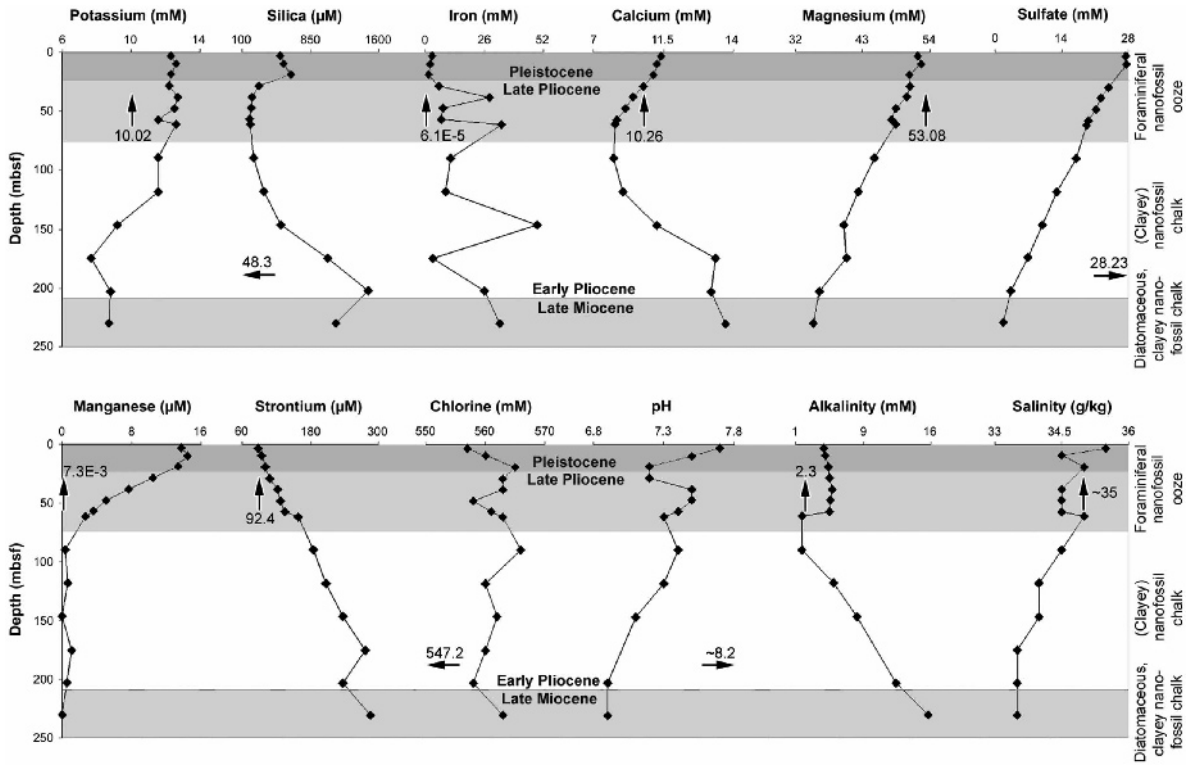


Figure 10. Interstitial solution profiles for ODP Site 959 (data from Mascle *et al.*, 1996). Average seawater composition (black arrows) based on Turekian (1968) and the lithology of Hole 959C are labeled for comparison.

trend which was interpreted by Mascle *et al.* (1996) as a dynamic redistribution of Fe within the sediment column.

The oxidation of marine organic matter and also sulfate reduction are likely to play a key role in regulating the pH of the interstitial solution, as indicated by the drop in pH from 7.7 to 7.2 in the first 20 mbsf (Figure 10) which reflects the formation of *e.g.* carboxylic acids and $H_2S$ (Mascle *et al.*, 1996). At this site, the interstitial solution pH is buffered by calcium carbonate dissolution, as documented by the increase in total alkalinity and $Sr^{2+}$ content. Hence, the pH within organic-rich micro-environments such as in the biofilm within foraminifera tests is probably much lower (pH <5) than that of the interstitial solution. Such locally occurring acidic conditions can promote dissolution of detrital silicates such as feldspar, as documented by the present XRD and SEM data (Figures 3, 4). As a consequence, the concentration of silicic acid in the interstitial solution increases with burial depth (Figure 10), reaching a first maximum at 20 mbsf (~650 μM). Alterations of bio-opal and clay minerals (Figure 4) provide additional ions such as $Al^{3+}$, $Fe^{2+}$, $Na^{+}$, $Ca^{2+}$, and $Mg^{2+}$ (*e.g.* MacKenzie, 2005) that are required for ongoing glauconitization.

Due to intense silicate weathering, the $K^{+}$ concentration of the interstitial solution (Figure 10) in the first 50 mbsf (12.2−12.7 mM) is ~20−25% greater than that of seawater (10.02 mM) but it decreases continuously below 120 mbsf. An elevated $K^{+}$ concentration of the interstitial solution probably favors the glauconitization reaction by irreversible $K^{+}$ fixation, as indicated by the TEM-EDX data and by previous studies on the illitization of smectite (Hower *et al.*, 1976; Kaufhold and Dohrmann, 2010).

In summary, the interstitial solution chemistry at ODP Site 959 was modified by early diagenetic silicate mineral alteration, microbial sulfate reduction, Fe redox reactions, carbonate dissolution, and oxidation of organic matter, and is probably the driving force for glauconitization within the sedimentary pile.

### *Rate of deep-water glauconitization*

At the ODP Site 959, Fe-smectite formation is considered to be the initial step to glauconitization which occurred in semi-confined, organic-rich micro-environments, as provided within the tests of foraminifera. According to chemical modeling of Fe-smectite formation in deep-sea sediments from the Costa Rica margin (Charpentier *et al.*, 2011), several thousands of years are required to precipitate Fe-smectite in large quantities. Gaudin *et al.* (2005) suggested that these neo-formed Fe-smectites are thermodynamically unstable during early marine diagenesis and alter rapidly into glauconite *via* Gl-S formation. Evidence for such a progressive Fe-smectite into glauconite alteration is

https://doi.org/10.1346/CCMN.2013.0610307 Published online by Cambridge University Press

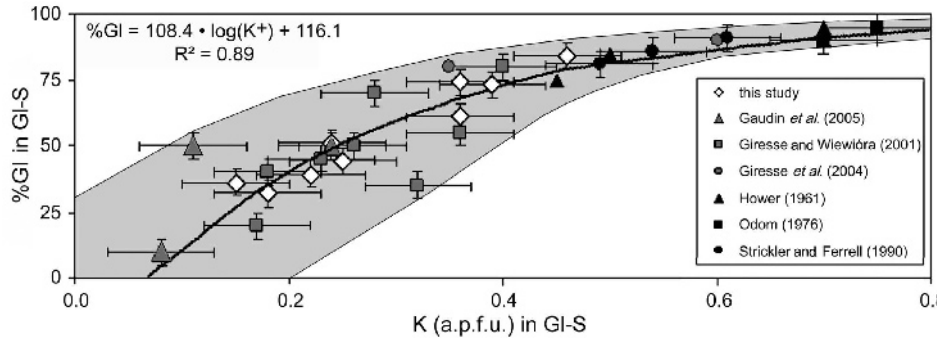


Figure 11. Relationship between %Gl and interlayer $K^+$ content in Gl-S. Glauconite formation is accompanied by a continuous $K^+$ uptake.

given by the positive correlation ($R^2 = 0.89$) between the increasing percentage of %Gl in Gl-S and the associated higher $K^+$ content per a.p.f.u. (Figure 11) with grain maturity, according to the expression:

$$\%Gl = 108.4 \cdot \log(K^+) + 116.1 \text{ for } K^+ < 0.7 \text{ a.p.f.u.} \quad (1)$$

The proportion of %Gl in Gl-S of the total green grains at a given depth, namely, the state of overall glauconitization in the sediment ($\%Gl_{Sed}$), was calculated with equation 1 using the average K content (± 0.05 K a.p.f.u.) of each green-grain sub-fraction (Table 1) multiplied by its percentage (±5%) in the total green-grain fraction from each depth (Figure 5). These calculations revealed 30, 60, and 75% $Gl_{Sed}$, each ± 10%, at 0.16, 11.69, and 24.91 mbsf which correspond to sediment ages of ~10, 900, and 2500 ky, respectively, given by Giresse and Wiewióra (2001). Assuming that the formation of Fe-smectite with initially little if any %Gl requires ~1 ky (Charpentier *et al.*, 2011), an average glauconitization rate for the ODP Site 959 can be obtained by plotting ($R^2 = 0.97$) the $\%Gl_{Sed}$ against the age of the sediment ($age_{Sed}$ in ky), according to the equation:

$$\%Gl_{Sed} = 22.6 \cdot \log(age_{Sed}) + 1.6 \text{ for } age_{Sed} < 10 \text{ My} \quad (2)$$

The glauconitization rate in this modern deep-sea environment (ODP Site 959) is about five times less than that in the shallow shelf (*e.g.* Odin and Fullagar, 1988) which probably reflects the lower temperatures (~3−6ºC) and the limited supply and reflux of essential cations which are required for glauconitization such as Fe, $K^+$, $Mg^{2+}$, and silica. However, the rate of deep-sea glauconite formation is significantly faster than that of smectite illitization that occurs during burial diagenesis (*e.g.* Hower *et al.*, 1976), which may reflect the role of Fe, as shown by the positive linear correlation ($R^2 = 0.98$) between the increasing $Fe_2O_3$ content and the associated higher percentages of %Gl in Gl-S (Figure 12).

As previously suggested by Baldermann *et al*. (2012), the availability of Fe and subsequently the extent of $Fe^{3+/2+}/Mg^{2+}$ for $Al^{3+}$ substitutions in the octahedral sheet of the neo-formed Fe-smectite and related Gl-S is

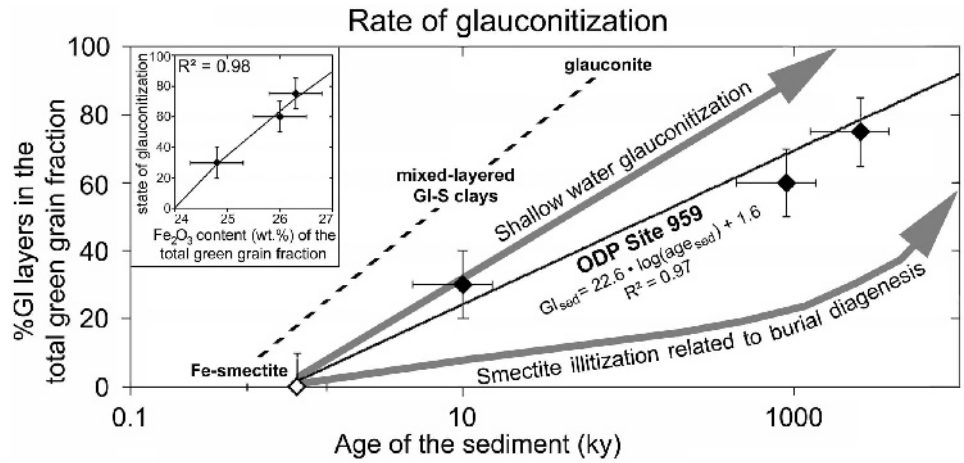


Figure 12. Glauconitization rate for the ODP Site 959. The positive, linear correlation between increasing Fe content and the state of glauconitization implies that Fe could be the overall rate-limiting element (inserted box). The rate of shallow-water glauconitization, as suggested by Odin and Fullagar (1988), and the rate of illitization of smectite, as proposed by Hower *et al*. (1976) for the Gulf Coast sediments, are included for comparison.

https://doi.org/10.1346/CCMN.2013.0610307 Published online by Cambridge University Press

expected to have a major impact on the rate of glauconitization. With increasing proportion of bivalent octahedral cations such as $Fe^{2+}$ and $Mg^{2+}$ the octahedral charge increases and $K^+$ is progressively fixed into the interlayer sites to balance charge, as documented by the TEM-EDX compositions of the Ivory Coast glauconites and Gl-S (Table 1). The proportion of $Fe^{2+}$ in the green grains could not be determined in the present study due to the small amount of green grains available. However, the greening of the grain color with increasing burial depth indicates that some $Fe^{2+}$ in the structural formulae of Gl-S is probable. Thus, the progressive fixation of Fe as well as Fe reduction during glauconitization is considered to be a likely rate-controlling factor, as expressed in the linear relationship of increasing $Fe_2O_3$ contents and the state of glauconitization (Figure 12).

*Model for deep-water glauconite formation*

As a result of the petrographic, mineralogical, and chemical observations in the present study, the glauconitization process of foraminifera tests at ODP Site 959 is proposed to occur in three steps (Figure 13):

(1) After sedimentation (~0.01–1 ky), most of the marine organic matter was oxidized. This resulted in locally reducing and slightly acidic conditions ($pH_\mu < pH_{Sed} < pH_{sw}$) in the micro-environment of glauconitization ($pH_\mu$) and the surrounding sediment ($pH_{Sed}$) compared to the seawater pH ($pH_{sw}$), as documented by the interstitial solution data (Figure 10). Such conditions favored the dissolution of carbonate, bio-opal, and silicate minerals (*e.g.* Raiswell and Canfield, 2012), making dissolved $K^+$, $Mg^{2+}$, and silica readily available at the ODP Site 959. However, the mobilization and transport of Al and (in particular) Fe were probable limiting factors for the advance of glauconitization (Figure 12). Iron and Al are virtually absent from aquatic systems at seawater pH and at the analyzed pH of the interstitial solutions (*e.g.* Turekian, 1968). One key mechanism for the mobilization of Fe and Al is the microbial oxidation of biodegradable (marine) organic matter within the foraminifera tests which is expected to reduce the pH by the supply of *e.g.* carboxylic acids (MacKenzie, 2005). At pH<5 the solubility of FeO-OH and Al-O-OH significantly increases through the predominance of aqueous $Fe(OH)^{2+}$ and $Al(H_2O)_6^{3+}$ species in the $Fe_2O_3$–$Al_2O_3$–$H_2O$ system. The occurrence of Fe- and Al-containing organic aquo-complexes is enhanced under such conditions (*e.g.* McBride, 1994; Tipping, 2002).

(2) Immediately after the biodegradable marine organic matter was oxidized, the bacterial activity decreased, as indicated by the TEM observations (Figure 8), and an oxidation front developed in the tests of foraminifera (Gaudin *et al.*, 2005). This initiates a local micro-environment suitable for glauconitization. In the presence of an expanding oxidation front, rapid degradation of Fe- and Al-organic aquo-complexes could take place and $Fe^{2+}$ and $Al^{3+}$ cations were released temporarily. Accompanied by the constant re-oxidation of $Fe^{2+}$ to $Fe^{3+}$ and rapid $Al^{3+}$ supply, the formation of gel occurred contemporaneously with direct precipitation from bacterial biofilm. Subsequently, Fe-smectite formed within the amorphous precursor gels (Figure 8), initiated by the continuous cation supply from the surrounding sediment by chemical diffusion at moderate pH ($pH_\mu \approx pH_{sw} > pH_{Sed}$) (see Martín-Algarra and Sánchez-Navas, 1995). Charpentier *et al.* (2011) suggested that ~1–10 ky are required for the quantitative precipitation of Fe-smectite in deep-sea, low-temperature environments.

(3) The Fe-smectite-to-glauconite reaction was finally promoted by diffusion-controlled cation exchange between the micromilieu and interstitial solutions ($pH_\mu < pH_{Sed}$; Eh ≈ 0 mV), whereby both the initial sediment and the micro-environment of glauconitization became modified by several early diagenetic dissolution and replacement reactions, as described above. As dissolved $K^+$, $Mg^{2+}$, and silica are considered to have always been present in the interstitial solutions (Figure 10), the availability of Fe is suggested to be the most important rate-limiting factor for glauconitization of the Ivory Coast sediments. As soon as the Fe supply stopped, *e.g.* by changes in the pH and Eh conditions within the micro-environment of glauconitization, the Fe-smectite-to-glauconite reaction also stopped. Such unsuitable conditions for the formation of glauconite could occur locally within the same micromilieu such as within one single foraminifera test, a feature which explains why green grains with varying color, reflecting a divergent state of maturity, are present within the same horizon.

The physical properties of the sediment such as porosity, permeability, and tortuosity appear to have been additional key factors for glauconitization, by influencing the interstitial solution chemistry and its exchange with the micro-environment *via* diffusion. Changes in the rate of diffusion in the micro-environment, especially that of Fe and K, due to the loss of porosity and connectivity of pore space (Figure 7c,f), may explain why the glauconitization rate slows down with increasing burial depth and aging of the sediment (Figure 12). A reduced diffusion rate may also imply that as glauconization progresses the rate of $K^+$ fixation in Gl-S is relatively enhanced compared to the rate of formation of new Fe-smectite layers which can explain the logarithmic relationship between increasing %Gl in Gl-S and K content (Figure 11). This feature is probably attributed to the low thermodynamic stability of the Fe-smectite precursors (Gaudin *et al.*, 2005). Thus, the rate of glauconitization does decrease with increasing burial depth and subsequent aging of the original sediments, and at these low temperatures the process requires ~10 My to complete in the deep-water environment of the ODP Site 959, compared to <2 My in a shallow-water setting (Odin and Fullagar, 1988).

https://doi.org/10.1346/CCMN.2013.0610307 Published online by Cambridge University Press

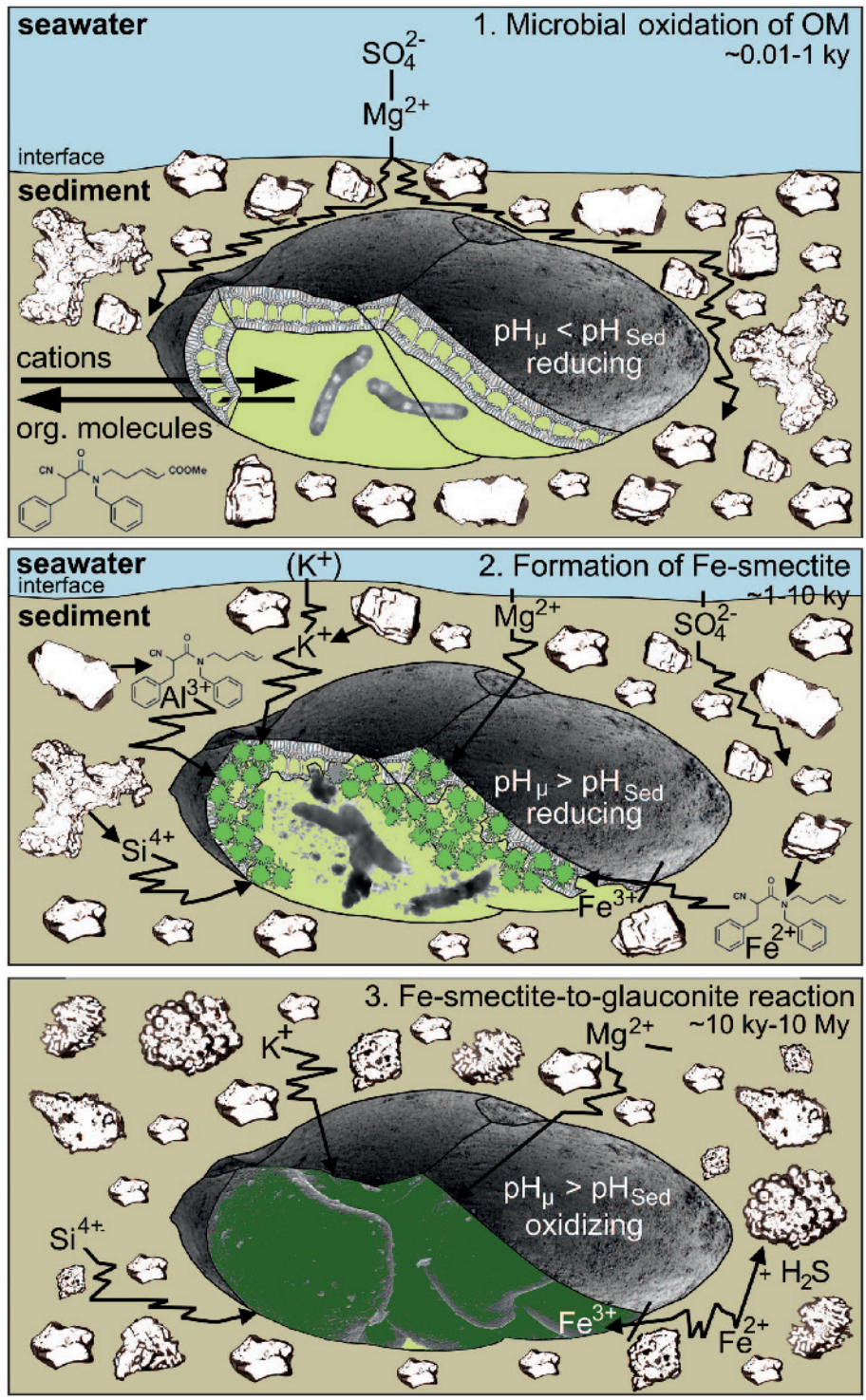


Figure 13. Glauconitization model for ODP Site 959. (1) Microbial oxidation of organic matter (OM) generates locally occurring reducing and acidic conditions in the micro-environment of glauconitization such as in foraminifera tests and the surrounding sediment. These conditions enhance (silicate) mineral dissolution and the formation of cation-organic aquo-complexes. (2) As soon as the OM is consumed, oxidation of the organic complexes and of $Fe^{2+}$ occurs. Subsequently, Fe-smectite formation takes place which is promoted by microbial activity and cation supply from the interstitial solution, while dissolution of skeletal calcite buffers the pH. (3) The Fe-smectite-to-glauconite reaction is controlled by the composition of the bulk interstitial solution and requires ~10 My to complete.

https://doi.org/10.1346/CCMN.2013.0610307 Published online by Cambridge University Press

## SUMMARY AND CONCLUSIONS

Authigenic, green glauconitic grains, formed in the recent deep-sea environment (~2100 m) of the ODP Site 959, Ivory Coast–Ghana Marginal Ridge, were studied in order to characterize the key factors controlling the rate and mechanism of deep-sea glauconite formation at low temperatures (~3–6ºC). The following conclusions were reached:

(1) Glauconitization occurred mainly in calcareous, planktonic, and benthic foraminifera tests. These semi-confined, organic-rich micro-environments provided the post-depositional conditions suitable for glauconitization. (2) XRD, TEM, and FIB-SEM results of the unaltered light green grains from 0.16 mbsf revealed dioctahedral Fe-smectites as the precursor phases for glauconite formation. These Fe-smectites were formed by precipitation from amorphous gels containing Fe, Mg, Al, and silica generated preferentially from microbial biofilm with cations supplied by diffusion from interstitial solutions. (3) During the later stages of early marine diagenesis, the neo-formed Fe-smectites changed into Gl-S and finally into glauconite with no recognizable compositional gaps between the Fe-smectite and glauconite end members, as identified by combined *Sybilla*© modeling, XRD, TEM-EDX, and TEM-SAED analysis. (4) The composition of the interstitial solution was influenced heavily by microbial oxidation of marine organic matter, Fe-redox reactions, and silicate and carbonate mineral weathering, as indicated by the SEM and hydrochemical results, and all of these early diagenetic alteration processes were important for maintaining glauconitization within the sediment pile. (5) The rate of deep-water glauconite formation depended mainly on continuous Fe supply but, due to the low-temperature conditions, the rate of reaction was about five times less than that in shallow-shelf regions.

## ACKNOWLEDGMENTS

The authors are grateful to A. Deditius and C. Nickel (Graz University of Technology) for their helpful contributions and suggestions during preparation of an early version of the manuscript. M. Zander (Ernst-Moritz-Arndt University of Greifswald) is acknowledged for technical assistance with the TEM and FIB-SEM analyses. Special thanks to J. Cuadros, J.M. Wampler, R. Dohrmann, J. Stucki, and an anonymous reviewer for their detailed comments which significantly improved the quality of this paper.

## REFERENCES

Bailey, S.W., Alietti, A., Brindley, G.W., Formosa, M.L.L., Jasmund, K., Konta, J., MacKenzie, R.C., Nagasawa, K., Raussell-Colom, R.A., and Zvyagin, B.B. (1980) Summary of the recommendations of the AIPEA nomenclature committee. *Clays and Clay Minerals*, **28**, 73–78.

Baldermann, A. (2012) Recent glauconite formation in a deep sea environment from ODP Site 959, Ivory Caost-Ghana Marginal Ridge. Masters thesis, Univ. Greifswald, Greifswald, Germany, 75 pp.

Baldermann, A., Grathoff, G.H., and Nickel, C. (2012) Micromilieu-controlled glauconitization in fecal pellets at Oker (Central Germany). *Clay Minerals*, **47**, 513–538.

Buatier, M., Honnorez, J., and Ehret, G. (1989) Fe-smectite-glauconite transition in hydrothermal clays from the Galapagos Spreading Center. *Clays and Clay Minerals*, **37**, 532–541.

Chaerun, S.K. and Tazaki, K. (2005) How kaolinite plays an essential role in remediating oil-polluted seawater. *Clay Minerals*, **40**, 481–491.

Charpentier, D., Buatier, M., Jacquot, E., Gaudin, A., and Wheat, C.G. (2011) Conditions and mechanism for the formation of iron-rich montmorillonite in deep sea sediments (Costa Rica margin): Coupling high-resolution mineralogical characterization and geochemical modeling. *Geochimica et Cosmochimica Acta*, **75**, 1397–1410.

Cuadros, J., Dekov, V.M., Arroyo, X., and Nieto, F. (2011) Smectite formation in submarine hydrothermal sediments: samples from the HMS Challenger Expedition (1872–1776). *Clays and Clay Minerals*, **59**, 147–164.

Gaudin, A., Buatier, M., Beaufort, D., Petit, S., Grauby, O., and Decareau A. (2005) Characterization and origin of $Fe^{3+}$-montmorillonite in deep water calcareous sediments (Pacific Ocean, Costa Rica margin). *Clays and Clay Minerals*, **53**, 452–465.

Giresse, P. and Wiewióra, A. (2001) Stratigraphic condensed deposition and diagenetic evolution of green clay minerals in deep water sediments on the Ivory Coast-Ghana Ridge. *Marine Geology*, **179**, 51–70.

Giresse, P., Gadel, F., Serve, L., and Barusseau, J.P. (1998) Indicators of climate and sediment-source variations at site 959: implications for the reconstructions of paleoenvironments in the Gulf of Guinea through Pleistocene times. *Proceedings of the Ocean Drilling Program, Scientific Results*, **159**, 585–603.

Giresse, P., Wiewióra, A., and Grabska, D. (2004) Glauconitization processes in the northwestern Mediterranean (Gulf of Lions). *Clay Minerals*, **39**, 57–73.

Harder, H. (1980) Synthesis of glauconite at surface temperatures. *Clays and Clay Minerals*, **28**, 217–222.

Hower, J. (1961) Some factors concerning the nature and origin of glauconite. *American Mineralogist*, **46**, 313–334.

Hower, J., Eslinger, E.V., Hower, M.E., and Perry, E.A. (1976) Mechanism of burial metamorphism of argillaceous sediments: 1. Mineralogical and chemical evidence. *Geological Society of America Bulletin*, **87**, 725–737.

Jimenez-Millan, J., Molina, J.M., Nieto, L., Nieto, M., and Ruiz-Ortis, P.A. (1998) Glauconite and phosphate peloids in Mesozoic carbonate sediments (Eastern Subbetic Zone, Betic Cordilleras, SE Spain). *Clay Minerals*, **33**, 547–559.

Kaufhold, S. and Dohrmann, R. (2010) Stability of bentonites in salt solutions: II. Potassium chloride solution – Initial step of illitization? *Applied Clay Science*, **49**, 98–107.

Keller, L.M., Holzer, L., Wepf, R., and Gasser, P. (2011) 3D geometry and topology of pore pathways in Opalinus clay: Implications for mass transport. *Applied Clay Science*, **52**, 85–95.

Kloprogge, J.T., Komarneni, S., and Amonette, J.E. (1999) Synthesis of smectite clay minerals: A critical review. *Clays and Clay Minerals*, **47**, 529–554.

Konhauser, K.O. and Urrutia, M.M. (1999) Bacterial clay authigenesis: a common biogeochemical process. *Chemical Geology*, **161**, 399–413.

Köster, H.M., Ehrlicher, U., Gilg, H.A., Jordan, R., Murad, E., and Onnich, K. (1999) Mineralogical and chemical characteristics of five nontronite and Fe-rich smectites. *Clay Minerals*, **34**, 579–599.

MacKenzie, F.T. (2005) *Sediments, Diagenesis, and*

*Sedimentary Rocks, 7: Treatise on Geochemistry*. Elsevier Science and Technology, USA.

Martín-Algarra, A. and Sánchez-Navas, A. (1995) Phosphate stromatolites from condensed cephalopod limestones, Upper Jurassic, southern Spain. *Sedimentology*, **42**, 893–919.

Mascle, J., Lohmann, G.P., Clift, P.D., *et al*. (1996) 9. Principal Results. *Proceedings of the Ocean Drilling Program*, *Initial Reports*, **159**, 297–314.

McBride, M.B. (1994) *Environmental Chemistry of Soils*. Oxford University Press, New York.

Meunier, A. and El Albani, A.E. (2007) The glauconite-Fe-illite-Fe-smectite problem: a critical review. *Terra Nova*, **19**, 95–104.

Moore, D. and Reynolds, R.C. Jr (1997) *X-ray Diffraction and the Identification and Analysis of Clay Minerals*. Oxford University Press, USA.

Norris, R.D. (1998) Planktonic foraminifer biostratigraphy: eastern equatorial Atlantic. *Proceedings of the Ocean Drilling Program, Scientific Results*, **159**, 445–479.

Odin, G.S. and Fullagar, P.D. (1988) Geological significance of the glaucony facies. Pp. 295–332 in: *Green Marine Clays* (G.S. Odin, editor). Elsevier, Amsterdam.

Odin, G.S. and Matter, A. (1981) De glauconiarum origine. *Sedimentology*, **28**, 611–641.

Odom, E. (1976) Microstructure, mineralogy and chemistry of Cambrian glauconite pellets and glauconite, central USA. *Clays and Clay Minerals*, **24**, 232–238.

Raiswell, R. and Canfield, D.E. (2012) The iron biogeochemical cycle past and present. *Geochemical Perspectives*, **1**, 1–222.

Schulz, H.D. and Zabel, M. (2006) *Marine Geochemistry*. Springer, Berlin.

Strickler, M.E. and Ferrell, R.E., Jr (1990) Fe substitution for Al in glauconite with increasing diagenesis in the first Wilcox sandstone (Lower Eocene), Livingston Parish, Lousiana. *Clays and Clay Minerals*, **38**, 69–76.

Tipping, E. (2002) *Cation Binding by Humic Substances*. Cambridge University Press, Cambridge, UK.

Turekian, K.K. (1968) *Oceans*. Prentice Hall, New Jersey, USA.

Wagner, T. (1998) Pliocene-Pleistocene deposition of carbonate and organic carbon at Site 959: Paleoenvironmental implications for the eastern equatorial Atlantic of the Ivory Coast/Ghana. *Proceedings of the Ocean Drilling Program, Scientific Results*, **159**, 557–574.

Warr, L.N. and Grathoff, G. (2012) Geoscientific applications of particle detection and imaging techniques with special focus on the monitoring clay mineral reactions. Pp. 667–683 in: *Handbook of Particle Detection* (C. Grupen and I. Buvat, editors). Springer, Berlin.

Warr, L.N., Perdrial, J.N., Lett, M.-C., Heinrich-Salmeron, A., and Khodja, M. (2009) Clay mineral-enhanced bioremediation of marine oil pollution. *Applied Clay Science*, **46**, 337–345.

Wiewióra, A., Giresse, P., Petit, S., and Wilamowski, A. (2001) A deep-water glauconitization process on the Ivory Coast–Ghana Marginal Ridge (ODP Site 959): Determination of $Fe^{3+}$-rich montmorillonite in green grains. *Clays and Clay Minerals*, **49**, 540–558.

(*Received 24 January 2013; revised 11 May 2013; Ms. 741; AE: R. Dohrmann*)